

1.3 mm² Nav-Grade NEMS-based Gyroscope

Marco Gadola, Andrea Buffoli, Marc Sansa, Audrey Berthelot, Philippe Robert,
and Giacomo Langfelder, *Member, IEEE*

Abstract— The research reports the design and experimental results of novel gyroscopes based on nano-resistive sensing, capable to meet navigation grade specifications within a sensor footprint of 1.3 mm² and a total silicon structural volume of 0.026 mm³ only. A significant increase of the scale-factor is obtained through a combination of (i) optimization of the Coriolis force transduction into a stress on the resistive gauges, (ii) increase of the drive motion amplitude and (iii) increase of the current through the sensing gauges. Combined with low-pressure eutectic packaging, this enables approaching the thermomechanical noise limits of the sensor at about 0.004 °/√hr. At the same time, electronics is developed with minimum demodulation phase errors, thus enabling optimized closed-loop quadrature compensation and minimization of drift effects. Thanks to the inherent rejection of parasitic couplings and associated drifts of the used technology, the overall stability reaches 0.02 °/hr on average on 6 samples. These performances are demonstrated for a 30-Hz system bandwidth and few hundred dps input range over several samples. Navigation grade performance are confirmed by additional in-operation experiments like gyrocompassing and in-run 9-minute long angle measurements from rate integration.

Index Terms—gyroscopes, inertial navigation, NEMS, stability.

I. INTRODUCTION

THE myriad of applications enabled by low-noise, high-stability gyroscopes, including navigation in the virtual world (e.g. augmented reality [1]), navigation in the real world (e.g. autonomous driving [2]), and navigation towards outer worlds (e.g. cube satellites [3]), is pushing the development of miniaturized, lightweight, high-performance angular rate sensors. Planar microelectromechanical systems (MEMS) have been one candidate technology for more than a decade. At the state of the art, the most impressive results were achieved by using large-area devices with specialized packages and accurate calibration algorithms: (i) Challoner in [4] (Boeing gyroscope), used mode-matched disk resonator gyroscopes with a 8-mm diameter, reaching 0.0035 °/√hr angle random walk (ARW) and 0.012 °/hr uncompensated bias instability (BI) for an overall structural volume of about 6.4 mm³ and a vacuum-sealed LCC package volume of 1 cm³. Very similar performances were recently achieved by Xu et al. in [5] with a 8-mm diameter honeycomb disk structure; (ii) Edean in [6] (Honeywell gyroscope), relying on a mode-split capacitive gyroscope with calibration and post-acquisition compensation of environmental effects, showed 0.003 °/√hr noise and 0.01

°/hr stability in a 500 mm³ packaged volume; (iii) Koenig in [7] (Northrop Grumman gyroscope), using mode-matched sensors with special encapsulation (several cm³) for high-end applications, reached 0.016 °/√hr noise and 0.02 °/hr stability on average on ten different samples.

Recently, planar MEMS technology has been also challenged by 3D processes. Approaches based on fused-silica benefit from the low-loss structural material (glass re-blown technologies), reaching high quality factors (in the 10⁶ range), and representing a hybrid between micromechanical technologies and hemispherical resonator gyroscopes (HRG): in this framework, Singh demonstrated in [8] a micro-shell gyroscope with 0.0062 °/√hr ARW (not far from bulk HRGs [9]) and 0.027 °/hr BI within about 500 mm³ of overall structural volume. Another alternative technology under constant miniaturization is based on Nuclear Magnetic Resonance (NMR): in [10], Walker presented measurements of a NMR gyroscope fitting in 10 cm³ and reaching 0.005 °/√hr angle random walk and 0.02 °/hr stability. Table 1 summarizes these results, together with ARW and BI requirements for various gyroscope applications according to reference [7].

TABLE I
NAVIGATION GRADE MEMS AND NON-MEMS MINIATURIZED GYROSCOPES

AUTHOR	TYPE	ARW [°/√hr]	BI [°/hr]	ACTIVE VOLUME [mm ³]
Challoner [4]	Disk, capacitive, mode-match	0.0035	0.012	6.4*
Xu [5]	Honeycomb disk, mode- match	0.0048	0.015	5*
Edean [6]	Tuning fork, capacitive, mode-split	0.003	0.01	n.a.
Koenig [7]	Tuning fork, capacitive, mode-match	0.016	0.021	n.a.
Singh [8]	Glass re-blown HRG	0.0062	0.027	500
Walker [10]	Nuclear Magnetic Resonance	0.005	0.02	n.a.
This work	Tuning fork, NEMS, mode-split	0.004	0.02	0.03
Tactical grade**		0.05–0.5	0.15–15	low-volume means better C-SWaP
Navigation grade**		0.001–0.05	0.001–0.15	
Strategic grade**		<0.001	<0.001	

* value estimated from reference and assuming 100-μm silicon thickness [4-5]
** reference values taken from [7]

M. Sansa, A. Berthelot and P. Robert are with Univ. Grenoble Alpes, CEA, Leti, F-38000, Grenoble, France (e-mail: marc.sansaperna@cea.fr).

Manuscript first submitted for review on April, 6th, 2021.

M. Gadola, A. Buffoli and G. Langfelder are with Politecnico di Milano, 20133, Milano, Italy (e-mail: marco.gadola@polimi.it).

This work demonstrates that a technology based on resistive nano-MEMS (NEMS) can reach performance similar to the aforementioned examples, thus falling in the navigation-grade category, but within a 1.3 mm² footprint. From a theoretical standpoint, it is known that a high scale-factor, together with quadrature compensation, accurate demodulation phase (large quality factor) and minimization of parasitic effects (so, of their hardly predictable drifts) are key elements for low noise and improved stability. The technology used in this work, already disclosed in [11, 12], copes with all the listed requirements. Indeed, scale-factor values can be easily and independently programmed by trimming the bias current flowing through the NEMS gauges. This avoids any need for large voltages, typical of capacitive technologies, which unavoidably increase capacitive couplings, generate unwanted tuning and, in turn, determine undesired drifts due to second-order effects (tuning changes due to voltage drift, coupling changes due to parasitic drifts, ...).

The technology is here exploited in a newly proposed MEMS design, combining a tuning-fork architecture optimized for large drive displacement, mode-split operation at moderate split values, framed-levered sense-mode with amplification of stress effects on the sensing NEMS gauges, automatic quadrature compensation and large quality factors. The system electronics is also optimized towards minimization of phase errors and drifts, otherwise detrimental for quadrature leakage into the sense channel and in turn for stability. Temperature and bias drifts of the sensing elements are self-compensated by the closed-loop driving and open-loop sensing approach.

The proposed system reaches 0.004 °/√hr ARW and 0.02 °/hr stability on average over several tested samples, unrivaled results for a mm²-size gyroscope footprint. Accounting for the 20 μm process thickness, the overall volume enclosing the structural parts is of 0.03 mm³ only. This means that, within larger packages for specialized applications, one could fit several tens of such systems, potentially exploiting redundancy and cross-correlation techniques for additional performance improvements.

The next sections detail the theoretical background, the gyroscope and electronics design, and finally the characterization performed on several samples.

II. SYSTEM LEVEL ANALYSIS OF NOISE AND STABILITY

A. Noise in NEMS-based gyroscopes

Scale-factor SF (in SI units of [V/(rad/s)]) and angle random walk σ_n (in SI units of [rad/s/√Hz]) for a piezoresistive gyroscope, whose drive motion is controlled to an amplitude x_D by phase and gain loops, are given in the equation below [13]:

$$SF = \frac{V_{ref} \Gamma_S}{\Delta\omega \Gamma_D} \quad (1)$$

$$\sigma_n = \sqrt{\frac{k_B T b_s}{4(\omega_D m_S x_D)^2} + \frac{(4k_B T R_B + \sqrt{S_{Vn}}) G_{INA}^2}{SF^2}} \quad (2)$$

$$x_d i_B = V_{ref} \frac{2 A_g}{\rho \Gamma_D G_F G_{INA}} \quad (3)$$

In the scale-factor equation (1), V_{ref} is a reference voltage, which is used to set the drive motion amplitude x_D for a given gauge biasing current i_B . The ratio Γ_S/Γ_D represents a highly stable geometrical factor corresponding to the deamplification

of the drive and sense motion onto the NEMS gauges (as will be clarified later in the design subsection). The term $\Delta\omega = 2\pi\Delta f$ indicates the split value between the modes. G_F , A_g and ρ represent the gauge factor, cross-section, and resistivity, respectively. The reader can note how the scale-factor remains independent of the listed gauge parameters (and thus of their possible drifts) thanks to the self-compensation mechanism between drive and sense gauges described in [13]. The scale-factor remains, instead, dependent on the voltage value V_{ref} , which should thus be stable over time and temperature (e.g. a bandgap-generated reference).

In the first term of the ARW equation (2), $k_B T$ is the product of the Boltzmann constant and the absolute temperature, b_s is the damping coefficient of the sense mode, responsible of thermomechanical noise, and ω_D and m_S are the operating frequency and the sense modal mass. The factor 4 at the denominator accounts for the tuning fork structure and for the conversion between noise density and ARW. In the second term of the ARW, R_B represents the NEMS resistance and S_{Vn} is the noise density of the front-end amplifier having a gain G_{INA} .

Compared to a conventional capacitive gyroscope, one can note the absence of the rotor biasing voltage: this is usually a large value (15 V to 50 V, see e.g. [14, 15, 17]), which consequently eases parasitic capacitive couplings. Couplings may change in time and temperature especially in low-area devices for various reasons: change of distance between interconnections or bonding wires induced by bending, or variation of the dielectric properties of the capacitive coupling induced by humidity changes. Couplings are indeed a hardly predictable source of drift. The absence of large voltages in NEMS-based gyroscopes overcomes this issue.

The other major difference is the presence of the NEMS biasing current, included in the voltage V_{ref} (usually having maximum values of 1 V). This current can be independently regulated to obtain widely varying scale factors. In this research, gyroscopes were operated with values of gauge

TABLE II
DESIGN PARAMETERS

PARAMETER	SYMBOL	VALUE
Target mode split value	$\Delta\omega$	2π 150 Hz
Sense lever factor	Γ_S	$1.2 \cdot 10^{-1}$
Drive lever factor	Γ_D	$0.6 \cdot 10^{-5}$
Operating frequency	ω_D	2π 25 kHz
Sense modal mass	m_S	$3.5 \cdot 10^{-9}$ kg
Target drive displacement	x_D	9 μm
Drive mode quality factor	Q_D	50000
Sense mode quality factor	Q_S	20000
Gauge length	L_g	5 μm
Maximum gauge bias current	i_B	450 μA
Gauge factor	G_F	50
Gauge cross section	A_g	(250 nm) ²
Gauge resistivity	ρ	$3 \cdot 10^{-5}$ Ω·m
Reference voltage	V_{ref}	1.1 V
Circuit voltage swing	V_{DD}	4 V
Front-end amplifier gain	G_{INA}	35
Amplifier voltage noise density	$\sqrt{S_{Vn}}$	3 nv/√Hz

current in the order of few hundred μA . This value is large compared to consumer applications maximum current budget, but remains extremely low for high-end applications, guaranteeing a very favorable cost-size-weight and power (C-SWaP) figure of merit.

Nevertheless, for the typical parameters of a yaw gyroscope, as shown in Table II, a scale-factor at the front-end output around 5 mV/dps can be already obtained. At the same time, ARW in the order of 50-100 $\mu\text{dps}/\sqrt{\text{Hz}}$, corresponding to 0.003°-0.006 $^\circ/\sqrt{\text{hr}}$, can be reached, approaching the thermomechanical limit of the sensor.

B. Stability in NEMS-based gyroscopes

Among the various sources of zero-rate-output (ZRO) instability, leakage of quadrature Ω_q into the sense channel after demodulation errors ϕ_{er} , is a huge contribution due to possible drifts of both these terms. Other drifts may arise due to undesired couplings $o(T)$ and their fluctuations.

$$\text{ZRO}(T) \approx \phi_{er}(T) \Omega_q(T) + o(T) \quad (4)$$

Input referred quadrature Ω_q originates from electromechanical imperfections, in particular related to non-orthogonality between drive motion and the sense axis [16]. While it is known that quadrature can be compensated by suitable closed-loop circuits [14, 16], it has to be remarked that this compensation works well only if demodulation phase is properly retrieved, which is why an accurate and stable demodulation reference is mandatory. Phase error originates both in the mechanical domain and in the electronics domain. For mode-split operation, it can be shown that the phase change induced by a

Coriolis force on the motion of the sense frame takes the expression below:

$$\phi_{er}(T) = \frac{-f_{s0}(1+\alpha\Delta T)}{2\Delta f_{ds0}(1+\alpha\Delta T)} \frac{1}{Q_s(T)} = \frac{-f_{s0}}{2\Delta f_{ds0}} \frac{1}{Q_s(T)} \quad (5)$$

where f_{s0} and Δf_{ds0} are the sense mode frequency and mode split at a reference temperature, α is the temperature coefficient of frequency, and $Q_s(T)$ represents the sense mode quality factor. Clearly, large quality factors are beneficial to minimize this error. This is one main reason driving several works on ultra-large-quality-factor gyroscopes [17, 18].

Assuming this contribution is minimized, there is a further contribution to $\phi_{er}(T)$ in equation (4), related to the relative drifts arising in the electronics between the demodulation reference signal and the Coriolis/quadrature signals: in other words, the electronic front-end stages, with their own poles and zeros, introduce some non-negligible lag. From this standpoint, NEMS-based resistive gyroscopes, with identical front-end for the drive and sense chain, and void of parasitic couplings, are inherently more robust than their capacitive counterpart, thus minimizing the overall demodulation error, which leads to accurate quadrature compensation and bypass of their drifts.

III. GYROSCOPE AND ELECTRONICS DESIGN

Figure 1 highlights the use process. The fabrication steps include (a) NEMS gauge patterning on a silicon-on-insulator (SOI) wafer with 250-nm thick monocrystalline silicon layer (33 $\mu\Omega\cdot\text{m}$), (b) epitaxial growth, resulting in a structural layer thickness of 20 μm , (c) deep reactive ion etching with a 20:1 aspect ratio, followed by hydrofluoric acid release and (d) aluminum-germanium eutectic bonding to a cap wafer with patterned getter. More process details can be found in [17], with the sole difference that the newly adopted Al-Ge bonding guarantees pressures in the order of 200-400 μbar , yielding drive-mode and sense-mode quality factors up to $5\cdot 10^4$ and $2\cdot 10^4$, respectively.

Figure 2a presents a falsely colored microscope picture of the designed device, having a structural layer footprint of (1.45 · 0.91) mm^2 . Differences in the sensor with respect to former designs [13] in the same technology are listed below, with the aim of reaching the target performance discussed in Section II:

- the new design allows a maximum 12- μm drive stroke to the stoppers, targeting 9- μm maximum anti-phase displacement (twice the values of previous designs), forced by a push-pull scheme. With the addition of four 3-fold springs at the drive frame corners, the lever system used to deliver stress onto the gauges (Fig. 2b) takes here a minimum role in setting the drive-mode stiffness, allowing its independent optimization for signal maximization and corresponding minimization of drive loop phase noise. Mechanical nonlinearities, according to finite element simulations, contribute less than 0.15% to the overall stiffness (about 330 N/m) at the maximum displacement. Operating frequencies are set at 25 kHz;
- the Coriolis frame accommodates quadrature nulling electrodes (not implemented in [13]) and decouples the C-shaped drive frame from the latticework sensing lever;
- the lever also features a central, rectangular frame, which

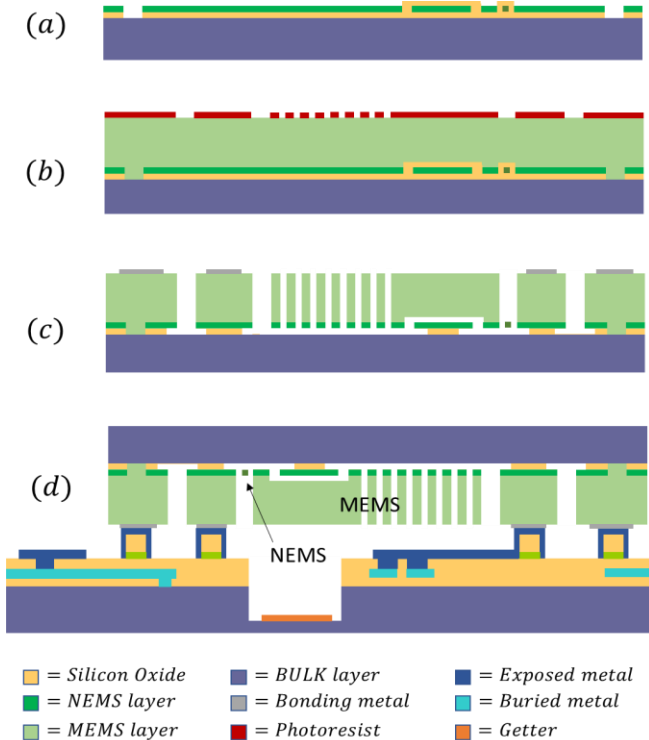


Fig. 1. Overview of the process fabrication. Starting from a SOI wafer, a monocrystalline silicon NEMS layer is first patterned (a) to define the NEMS gauges. All following steps are common to conventional MEMS processes, including epitaxial growth (b), ion etching and oxide release (c). The MEMS wafer is then bonded with a eutectic Al-Ge alloy to a cap wafer (d), where cavities and getters yield the final few-hundred μbar pressure.

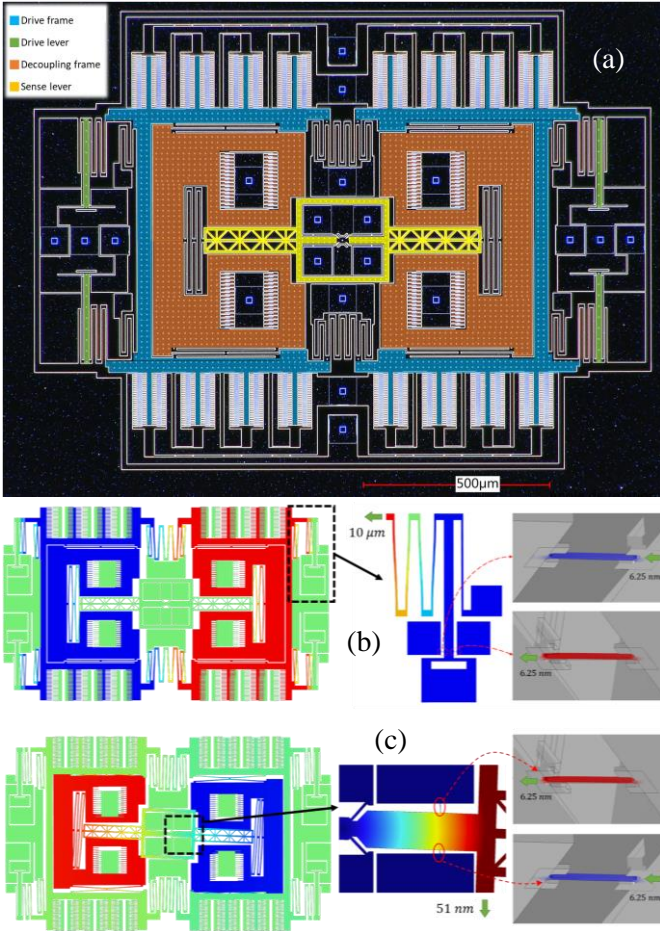


Fig. 2. Top-view image of the gyroscope (a), with false colors highlighting the drive and Coriolis frames and the corresponding decoupling levers. Their detailed operation can be understood through the modal shapes and the related zooms on the NEMS gauge region (b) and (c). The lever factors transduce different drive and sense motion amplitudes into the same maximum gauge elongation of 6.25 nm, corresponding to 200 MPa maximum stress.

minimizes lever deformations, thus guaranteeing an optimized stress transmission onto the sense-mode gauges (twice the value in [13]). These are located close to the hinge, as highlighted in Fig. 2c. The adopted lever design also shifts high-order modes towards larger frequencies, the first one occurring at 39.8 kHz.

The chosen mode-split value, nominally set at 150 Hz, varies between 60 Hz and 220 Hz due to fabrication nonuniformities, with an experimental example given in Fig. 3. For both the modes, dummy gauges are used to have a perfectly symmetric

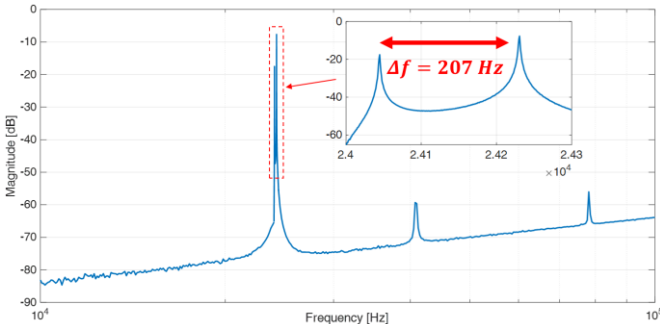


Fig. 3. Measured drive-to-sense spectrum showing the drive and sense modes (zoom) with about 200 Hz split. Visible spurious modes are at frequencies larger than 40 kHz and more than 50 dB below the main modes.

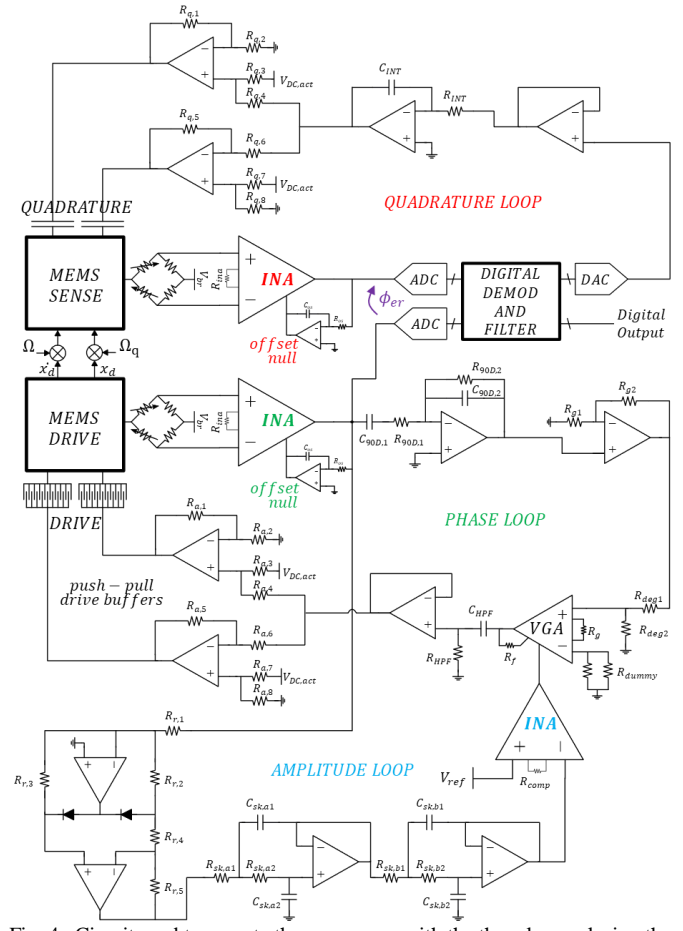


Fig. 4. Circuit used to operate the gyroscope, with the three loops closing the drive amplitude, drive phase and quadrature signal, and the open-loop sense chain in mode split operation.

device along the two in-plane axes. The active use of all gauges would bring advantages in terms of noise, at the same time increasing the overall current budget. While in this work this is avoided, it is not excluded that in future works one could take advantage of this concept to further improve noise performance.

The gyroscope is operated with the electronics shown in Fig. 4. Here the reader can recognize the two loops for drive motion control, with a primary phase loop based on an instrumentation amplifier front-end (INA with 35x gain), followed by an analog 90° phase shifter and a series of amplifying stages; and with a secondary, amplitude-control loop based on asynchronous rectifying and filtering. The control loop signal (the output of a second INA in the figure) drives a variable-gain amplifier (VGA model LMH6503 by Texas Instruments) that sets the drive AC voltage amplitude, nominally around 200 mV. This value is applied to the push-pull drive ports through a pair of buffers with opposite sign, and summed to a 3-V DC level.

The sense chain is readout in open-loop mode, with an INA front-end stage identical to the drive-loop one. This ensures that relative phase lags introduced by these stages are self-compensated, thus minimizing their contribution to ϕ_{er} (see Fig. 4) right before digital lock-in demodulation. With respect to the electronics in [12], further improvements are brought by:

- quadrature compensation in closed-loop feedback, through a proportional-integrator analog controller (R_{INT} , C_{INT} in the figure) and dedicated capacitive electrodes;

- offset nulling at the INA output of both the drive and sense loops. This allows increasing the NEMS gauge current to the nominal maximum value, without incurring in anticipated INA saturation due to DC imbalance of the NEMS gauge resistances.

The board operates at a 4-V supply without voltage boosting. The gauge current is set to 450 μA and drive motion is controlled to a target value of 9 μm by setting V_{ref} to 1.1 V. In these conditions, for a 150-Hz split value, the nominal scale-factor at the sense chain output is about 5.9 mV/dps, with theoretical noise contributions of 78 $\mu\text{dps}/\sqrt{\text{Hz}}$, 47 $\mu\text{dps}/\sqrt{\text{Hz}}$ and 23 $\mu\text{dps}/\sqrt{\text{Hz}}$ for the thermomechanical, Johnson and amplifier sources, respectively. This turns into a nominal ARW of 0.0057 $^{\circ}/\sqrt{\text{hr}}$. The system bandwidth is set to 30 Hz by the -80 dB/dec output digital low-pass filter.

IV. EXPERIMENTAL RESULTS

The board was mounted on a single-axis rate table (AC1120S from Acutronic). The system was initially tested as a function of the gauge current, demonstrating that the scale factor is easily and linearly programmed through this parameter (Fig. 5), reaching 6.6 mV/dps at the largest current, in fairly good agreement with predictions. In the latter condition, cross-axis rejection after accurate alignment of the system, orthogonal to

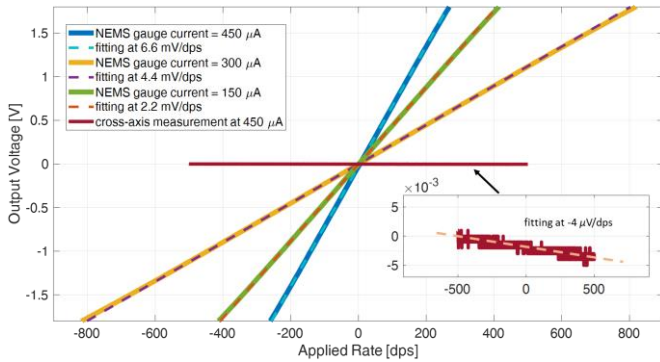


Fig. 5. Input-Output curve obtained for three different values of the NEMS gauge current, confirming the expected programmability of the scale-factor. The full-scale range is limited by the maximum ± 2 V input voltage range of the used lock-in amplifier. For the largest current value, a measurement obtained applying the rate orthogonal to the sensing axis demonstrates a cross-axis rejection larger than 64 dB.

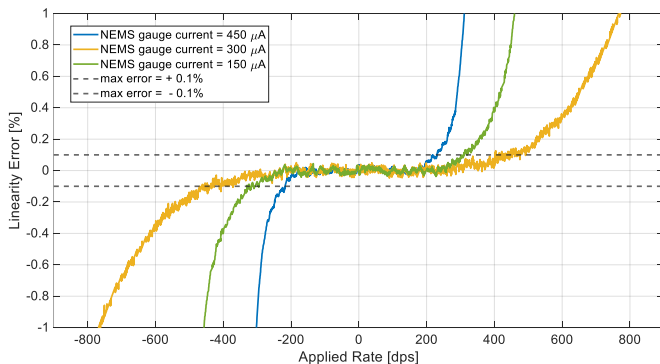


Fig. 6. Linearity error for different biasing currents and V_{ref} adjusted to have identical drive motion. The increased scale-factor at larger currents implies an early saturation of the output amplifier. The measured linearity errors are thus not to be ascribed to the NEMS gauges, which are always stressed by the same maximum stress in the three different situations.

the rotation rate, turns out to be as large as 64 dB. This is shown by the close-up in the same figure, with a cross-axis scale-factor fitting to as low as 4 $\mu\text{V}/\text{dps}$.

The extracted linearity error, shown in Fig. 6, is lower than 0.1 % up to 250 dps for the maximum current value. It is worth stressing that the linearity limit is here actually set by voltage saturation of the INA amplifier output voltage swing (limited to $V_{DD} - 2V = 2V$ for the INA163 by Texas Instruments), with no clear effect introduced by the sensing elements and by the current increase. We thus expect at least 1000-dps full-scale with sub-0.1% linearity error once the voltage supply of the electronics could be increased to about 10 V.

The static root Allan variance was then measured in uncontrolled laboratory environment ($\pm 2^{\circ}\text{C}$ maximum temperature variation), again as a function of the current (Fig. 7a). The figure demonstrates how a current increase brings both noise (as expected) and stability improvements, confirming no shortcomings due to the increased Joule effect dissipation through the gauges. Improvements are not linear with the inverse of the current, as noise levels are approaching the Brownian limit. Then, for the maximum current used in this work (450 μA), the test was repeated across several samples (Fig. 7b), demonstrating a well repeatable noise level in the order of 0.005 $^{\circ}/\sqrt{\text{hr}}$, with a record value of 0.0042 $^{\circ}/\sqrt{\text{hr}}$ for one sample with a slightly lower mismatch. At the same time, stability reaches in a pretty repeatable way values in the range of 0.014-0.029 $^{\circ}/\text{hr}$, which represents an unrivaled result for this

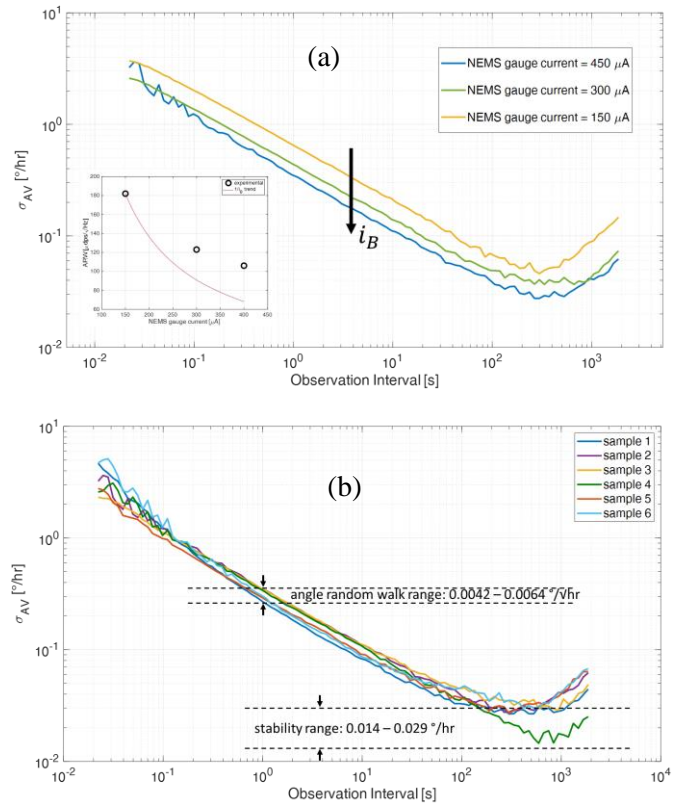


Fig. 7. 5-hr long root Allan variance of a sample device as a function of the NEMS gauge current (a). The less-than-inverse decrease of the ARW value, shown in the inset, indicates that the system is approaching thermomechanical limits, as predicted by theory. In (b), measurements on various samples captured at the largest current are shown, demonstrating a stability that well repeatably remains below 0.04 $^{\circ}/\text{hr}$ up to 1000 s.

TABLE III
PERFORMANCES OF DIFFERENT SAMPLES

SAMPLE N.	SPLIT [Hz]	ARW [$^{\circ}/\sqrt{\text{hr}}$]	AV minimum [$^{\circ}/\text{hr}$]
1	93	0.0042	0.026
2	217	0.0064	0.027
3	207	0.0057	0.028
4	146	0.0049	0.014
5	140	0.0046	0.027
6	61	0.0044	0.029

tiny gyroscope size, and, in general, among the best results for MEMS-based gyroscopes, even coping with navigation grade requirements. A results summary as a function of the mode-split value is given in Table III over the 6 tested samples.

It is interesting to note how a low split generally improves noise but has no significant effect on stability. One interpretation is that, though a small split value boosts the scale-factor and, in turn, lowers noise, output stability begins to be affected also by the stability of the split itself (Δf_{ds} vs temperature). Another possible drift source is the stability of the used V_{ref} reference.

Additional characterizations are then presented to proof that performances suggested by the root Allan variance graphs are held also in non-static operation. A 30-minute-long capture of Earth rotation in a gyrocompassing experiment [19] is shown in Fig. 8, along with the 4.16 mdps ($15^{\circ}/\text{hr}$) sinusoidal rate fitting.

Finally, a direct angle measurement in a 9-minute-long experiment is reported in Fig. 9. Here the gyro is calibrated at the startup for 1 second, to null initial offset, and used for angle estimation without any other calibration or compensation through Kalman filters. The residual angle error after such a long unbounded integration is lower than 0.1° (inset of Fig. 8), consistently with the Allan variance measurement and demonstrating no worsening effects of the gyro during operation, even under relatively large operating rates (200 dps peak-to-peak values). The error while the gyroscope is tilted by 360° is also shown in one of the close-ups. After 444-s integration, a small residual angle error is noted as the measured angle is 360.09° instead of the nominal 360° reference. The error is in the same range as the error around 0° , indicating that there is no significant additional effect brought by the scale factor nonidealities.

V. CONCLUSION

The work demonstrated the lowest-footprint gyroscope capable to reach navigation grade performance without any post-acquisition compensation of the measured angular rate. The key concept relies on the use of NEMS gauges where a high sensitivity is obtained through an optimized electromechanical design and the use of relatively large gauge biasing currents in the order of few hundred μA .

Operating in mode-split conditions, with closed-loop quadrature nulling but open-loop sense chain, experiments demonstrate sub- $0.04^{\circ}/\text{hr}$ stability at >1000 s observation interval on all tested samples, with an average ARW of $0.005^{\circ}/\sqrt{\text{hr}}$ in uncontrolled environment. This is obtained without lowering the gyroscope operating frequencies, which are kept

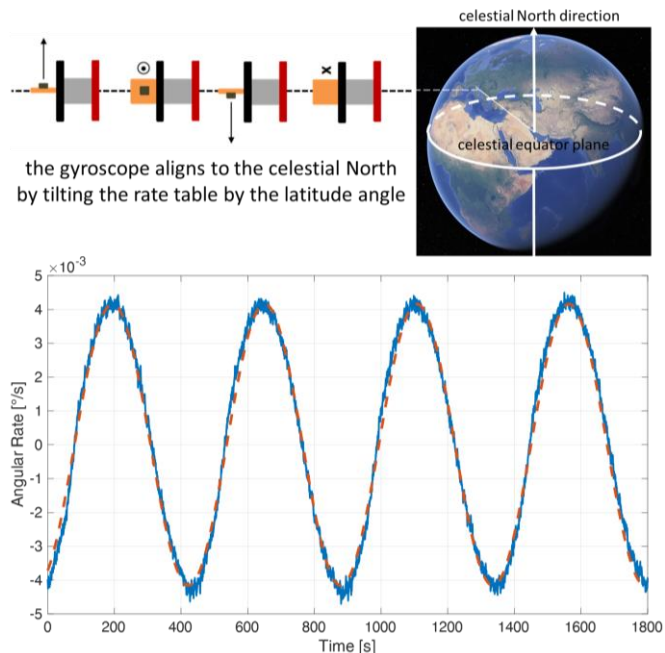


Fig. 8. 30-minute long gyrocompassing experiment under a 0.8 dps applied DC rate. The gyroscope measures the 4.16 mdps Earth rate, modulated by the relative change between the direction of the sensing axis and the celestial North pole direction as shown in the schematic setup above.

around 25 kHz (and first high order mode at 40 kHz), and with no post processing applied to raw captured rate data.

Such performances in such a low footprint stimulate the curiosity towards the development of N -gyroscope sensing units [20] while still coping with small overall volume and cost: in these systems, noise and stability can be further improved by combining the output of several (N) identical sensors, relying on Kalman filtering, averaging and cross-correlation methods. All of this is left for future research.

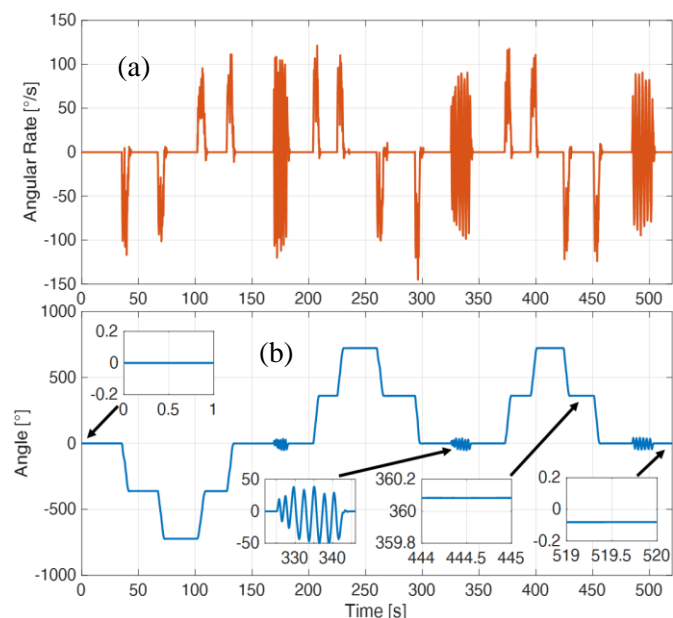


Fig. 9. Measured angular rate (a) and integrated angle (b) after 9-minute long in-operation navigation at 30-Hz bandwidth under manually applied angular motion. The gyro is repeatedly tilt by 180° constant angle rotations and by AC random motion with about 200-dps peak-to-peak value. The angle error at the end of navigation corresponds to 0.07° .

ACKNOWLEDGMENT

Authors would like to thank Dr. M. Allieri from Politecnico di Milano for her efforts in the electronic board development, and Dr. Thierry Verdoot from CEA, for his precious suggestions on the electromechanical gyroscope design.

REFERENCES

- [1] C. L. Hunt, A. Sharma, L. E. Osborn, R. R. Kaliki and N. V. Thakor, "Predictive trajectory estimation during rehabilitative tasks in augmented reality using inertial sensors," 2018 IEEE Biomedical Circuits and Systems Conference (BioCAS), Cleveland, OH, USA, 2018, pp. 1-4.
- [2] I. P. Prikhodko, B. Bearss, C. Merritt, J. Bergeron and C. Blackmer, "Towards self-navigating cars using MEMS IMU: Challenges and opportunities," 2018 IEEE International Symposium on Inertial Sensors and Systems (INERTIAL), Lake Como, Italy, 2018, pp. 1-4.
- [3] G. d. Alteriis, D. Accardo, R. S. Lo Moriello, R. Ruggiero and L. Angrisani, "Redundant configuration of low-cost inertial sensors for advanced navigation of small unmanned aerial systems," 2019 IEEE 5th International Workshop on Metrology for AeroSpace (MetroAeroSpace), Turin, Italy, 2019, pp. 672-676.
- [4] A. D. Challoner, H. H. Ge and J. Y. Liu, "Boeing Disc Resonator Gyroscope," 2014 IEEE/ION Position, Location and Navigation Symposium - PLANS 2014, Monterey, CA, USA, 2014, pp. 504-514.
- [5] Y. Xu *et al.*, "0.015 Degree-Per-Hour Honeycomb Disk Resonator Gyroscope," in *IEEE Sensors Journal*, vol. 21, no. 6, pp. 7326-7338, March 2021.
- [6] D. Endean *et al.*, "Near-Navigation Grade Tuning Fork MEMS Gyroscope," 2019 IEEE International Symposium on Inertial Sensors and Systems (INERTIAL), Naples, FL, USA, 2019, pp. 1-4.
- [7] S. Koenig *et al.*, "Towards a navigation grade Si-MEMS gyroscope," 2019 DGON Inertial Sensors and Systems (ISS), Braunschweig, Germany, 2019, pp. 1-18.
- [8] S. Singh, J. Woo, G. He, J. Y. Cho and K. Najafi, "0.0062 °/hr Angle Random Walk and 0.027 °/hr Bias Instability from a Micro-Shell Resonator Gyroscope with Surface Electrodes," 2020 IEEE 33rd International Conference on Micro Electro Mechanical Systems (MEMS), Vancouver, BC, Canada, 2020, pp. 737-740.
- [9] F. Delhay, "HRG by SAFRAN: The game-changing technology," 2018 IEEE International Symposium on Inertial Sensors and Systems (INERTIAL), Lake Como, Italy, 2018, pp. 1-4.
- [10] T. G. Walker, M. S. Larsen, "Spin-exchange-Pumped NMR Gyros," *Advances in Atomic, Molecular, and Optical Physics*, Volume 65, Chapter 8, 2016, pp. 373-401.
- [11] P. Robert *et al.*, "M&NEMS: A new approach for ultra-low cost 3D inertial sensor," *SENSORS*, 2009 IEEE, Christchurch, New Zealand, 2009, pp. 963-966.
- [12] S. Dellea, F. Giacci, A. F. Longoni, G. Langfelder, "In-Plane and Out-of-Plane MEMS Gyroscopes Based on Piezoresistive NEMS Detection," *Journal of Microelectromechanical Systems*, Vol. 24, No. 6, pp. 1817-1826, December 2015.
- [13] S. Dellea, P. Rey and G. Langfelder, "MEMS Gyroscopes Based on Piezoresistive NEMS Detection of Drive and Sense Motion," in *Journal of Microelectromechanical Systems*, vol. 26, no. 6, pp. 1389-1399, Dec. 2017.
- [14] E. Tatar, S. E. Alper and T. Akin, "Quadrature-Error Compensation and Corresponding Effects on the Performance of Fully Decoupled MEMS Gyroscopes," in *Journal of Microelectromechanical Systems*, vol. 21, no. 3, pp. 656-667, June 2012.
- [15] A. Sharma, M. F. Zaman and F. Ayazi, "A Sub-0.2°/hr Bias Drift Micromechanical Silicon Gyroscope With Automatic CMOS Mode-Matching," in *IEEE Journal of Solid-State Circuits*, vol. 44, no. 5, pp. 1593-1608, May 2009.
- [16] M. S. Weinberg and A. Kourepenis, "Error sources in in-plane silicon tuning-fork MEMS gyroscopes," in *Journal of Microelectromechanical Systems*, vol. 15, no. 3, pp. 479-491, June 2006.
- [17] S. Askari, M. H. Asadian, K. Kakavand and A. M. Shkel, "Vacuum sealed and getter activated MEMS Quad Mass Gyroscope demonstrating better than 1.2 million quality factor," 2016 IEEE International Symposium on Inertial Sensors and Systems, Laguna Beach, USA, 2016, pp. 142-143.
- [18] J. Chen, T. Tsukamoto and S. Tanaka, "Triple Mass Resonator with High Capacity to Tune Frequency and Quality Factor," 2020 IEEE

International Symposium on Inertial Sensors and Systems (INERTIAL), Hiroshima, Japan, 2020, pp. 1-4.

- [19] P. Prikhodko, S. A. Zotov, A. A. Trusov and A. M. Shkel, "What is MEMS Gyrocompassing? Comparative Analysis of Maytagging and Carouseling," in *Journal of Microelectromechanical Systems*, vol. 22, no. 6, pp. 1257-1266, Dec. 2013.
- [20] L. Blocher, "Purely Inertial Navigation With A Low-Cost MEMS Sensor Array," 2021 IEEE International Symposium on Inertial Sensors and Systems (INERTIAL), in press.



Marco Gadola received the B.Sc. and M.Sc. degrees in Electronics Engineering from Politecnico di Milano in 2015 and 2017, respectively. During his Master Thesis, he developed sensing electronic interfaces and several testing routines for MEMS Lorentz-force magnetometers. He is now a PhD candidate in Information technology at Politecnico di Milano, Italy, in collaboration with Cea-LETI, France, researching on 3-axis MEMS gyroscopes based on nano-gauge detection for high-stability applications.



Andrea Buffoli received the B. Sc. and M. Sc. in Electronics Engineering from Politecnico di Milano in 2018 and 2020, respectively. During his Master Thesis, he developed a low noise integrated circuit for MEMS gyroscopes based on nano-gauge detection. Dr. Buffoli is currently a research assistant working on characterization of M&NEMS gyroscopes for high performance and high stability applications.



Marc Sansa received the Ph.D. degree in Electronic Engineering from the Universitat Autònoma de Barcelona, Spain in 2013. He is currently a Research Engineer in the Sensors and Actuators Laboratory of the CEA-Leti in Grenoble, France, where he works on MEMS sensors and resonators. He has co-authored more than 40 publications and several patents in the field of MEMS.



Audrey Berthelot was born in Granville, France in 1974. She received the PhD in Materials Sciences from the University of Caen (France) in 2000. From 2000 to 2007, she worked as imagers and DRAM process integration engineer at Philips Semiconductors and NXP. Since 2007, she has led the development, the optimization and the industrialization of MEMS technologies in the French R&D Institute CEA.



Philippe Robert is business development manager and senior expert at CEA-Leti for MEMS sensors and actuators activities. After serving various positions in the sensor industry, he joined CEA-Leti in 2001 as project manager for RF-MEMS research and was promoted to manager of the MEMS

Sensors Group from 2003 to 2013, and head of the Microsystems Department from 2013 to 2019.

He holds a PhD in Electrical Engineering and a M.Sc. degree in Optical Electronic from Grenoble-INP.



Giacomo Langfelder (Member, IEEE) received the Ph.D. degree in Information Technology from the Politecnico di Milano, Milan, Italy, in 2009. He is currently an Associate Professor of “MEMS and Microsensors” and of “Electronics” with the Politecnico di Milano. He is the author

of about 150 publications and has applied for more than ten patents. His research interests include sensors, actuators and related electronics. Prof. Langfelder has been a member of the TPC of various IEEE conferences since 2016, and TPC chair of the IEEE Inertial conference in 2018.